Transient Characteristics and Physical Constraints of Grid-Tied Virtual Synchronous Machines

Chang Yuan[†], Chang Liu[**], Dan Yang[*], Ruibing Zhou[*], and Niang Tang[***]

[†,*]State Key Laboratory of Alternate Electrical Power System with Renewable Energy Sources,
North China Electric Power University, Beijing, China
[**]State Grid Jinan Power Supply Company, Jinan, China
[***]Electric Power Research Institute of Guangdong Power Grid Co., Ltd., Guangzhou, China

Abstract

In modern power systems, distributed generators (DGs) result in high stress on system frequency stability. Apart from the intermittent nature of DGs, most DGs do not contribute inertia or damping to systems. As a result, a new control method referred to as a virtual synchronous machine (VSM) has been proposed, which brought new characteristics to inverters such as synchronous machines (SM). DGs employing an energy storage system (ESS) provide inertia and damping through VSM control. Meanwhile, energy storage presents some physical constraints in the VSM implementation level. In this paper, a VSM mathematical model is built and analyzed. The dynamic responses of the output active power are presented when a step change in the frequency occurs. The influences of the inertia constant, damping factor and operating point on the ESS volume margins are investigated. In addition, physical constraints are proposed based on these analyses. The proposed physical constraints are simulated using PSCAD/EMTDC software and tested through RTDS experiment. Both simulation and RTDS test results verify the analysis.

I. INTRODUCTION

In order to alleviate environmental and energy supply problems, distributed generators (DGs) have been developing rapidly in recent years. In China, the installed capacities of grid-connected wind and solar power have reached 164GW and 130GW at the end of 2017, respectively [1]. In 2017, renewable energy generated 1.7 trillion kW·h of electricity, accounting for 26.4 percent of all the electricity generated [2]. In Europe, USA, Japan and India, significant targets have also been considered for the use of DGs and renewable energy sources in their power systems over the next two decades [3].

DGs employing grid connected power electronic converters result in high stress on power system frequency stability. Apart from the intermittent nature of DGs, most DGs do not contribute inertia or damping to systems. For example, wind turbines have an amount of kinetic energy stored in their blades, gear boxes and generators. However, they cannot support power systems directly. PV units do not have rotating parts that can be used as an energy buffer to deliver inertia to systems [4].

The inertia and damping in traditional power systems mainly come from synchronous machines. When frequency changes occur, the rotating masses inject or absorb energy into or from the grid to counteract the frequency variations in conventional power systems. Inertia in modern power systems can be defined as follows. Resistance in the form of energy exchange counteracts the frequency change, which results from an imbalance in the power generation and demand [4]. However, the equivalent rotating inertia of current power systems keeps decreasing due to the replacing of synchronous generators with DGs employing grid connected power electronic converters. The influences of decreasing inertia and damping on frequency stability are regarded as one of the main challenges in power systems.
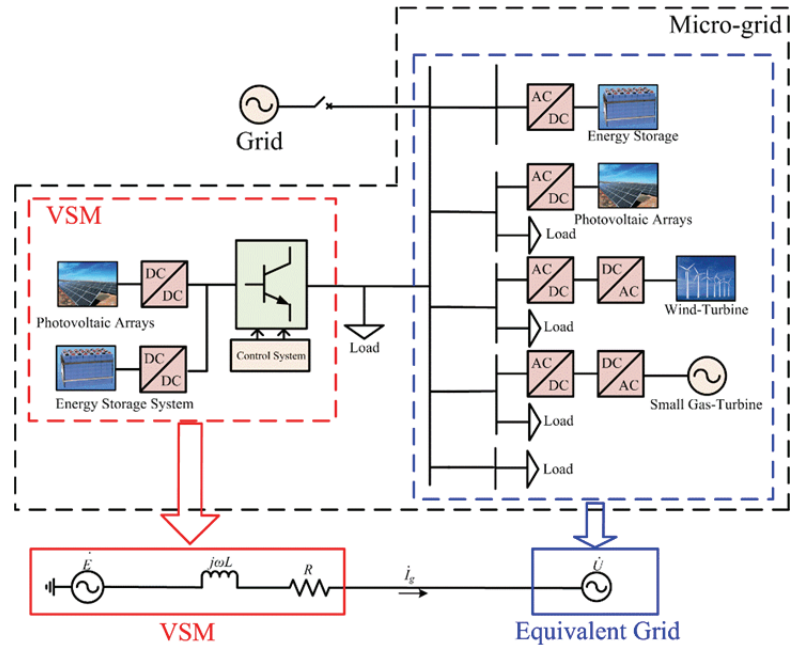
Fig. 1. System structure with VSM.

Virtual synchronous machines (VSMs) have become a promising method to solve frequency stability problems. VSM concepts and applications have been investigated in [5]-[8]. A VSM with an alternating moment of inertia was introduced in [9]. The authors of [10]-[12] mainly focused on optimal control strategies for the charging and discharging of ESS based on frequency variation detection. The authors of [13], [14] explored the utilization of energy storage devices to provide virtual inertia in order to maintain system stability. The virtual kinetic storage of VSMs has been investigated in [15] to maintain power system stability. Energy storage systems supporting a short-term frequency response have been studied in [16], [17]. The influences of different controller parameters and operating points on inertial dynamics have been discussed in [18] for VSMs. The relations between VSMs and frequency-droop control have been investigated in [19] and [20]. In addition, the static synchronous generator model proposed in [21] provided a new perspective to investigate grid-tied inverters.

There are two necessary conditions for inverters to provide inertia and damping to the system in this paper. First, the inverters should be controlled by a VSM. Second, energy storage should be implemented. An ESS operates to provide inertia and damping through charging or discharging when a frequency variation occurs. The volume of the ESS equipment is usually determined by investment, installation environment and other factors. Whether or not the VSM can provide enough inertia and damping to the system depends on the power and energy volume of the ESS equipment. However, the transient characteristics and physical constraints of the VSM have not been studied thoroughly. Thus, this

paper focuses on solving these issues.

This paper is organized as follows. In section II, a mathematical model of a VSM is built, and physical constraints are proposed. In section III, the quantitative relationships among the power and energy margins, the VSM key parameters and the operating points are studied. The simulation system configuration and detailed simulation results are presented in section IV. In section V, real-time RTDS experiments are carried out, and the transient characteristics of the VSM with different values of H and D are presented. Finally, some conclusions are presented in section VI.

II. ANALYSIS OF PHYSICAL CONSTRAINTS

A typical system structure of a VSM is shown in Fig. 1. In this section, a system structure with a VSM is presented, and a mathematical model of a VSM is built. The dynamic responses of the VSM output active power are investigated theoretically when the grid frequency steps. Physical constraints are proposed based on the analysis.

Microgrids have become a popular way to integrate DGs to the grid in low and medium voltage distribution systems. A typical system structure with a VSM is shown in Fig. 1. It includes a small gas turbine, a wind turbine, photovoltaic arrays, an ESS and different loads. In addition, the system can be operated either in a stand-alone fashion or while connected with the power grid. Inverters employing a VSM control can provide inertia and damping to systems. They can also mitigate frequency variations in the grid.

The VSM system in Fig. 1 contains PVs, ESSs and inverters.

It is known that PV units do not have rotating parts and contribute no inertia or damping to a system. An ESS can operate to provide inertia and damping through charging or discharging. The electromechanical energy conversion process is realized by an inverter employing VSM control.

A theoretical analysis and simulations are carried out by considering the following conditions and assumptions.

(1) The pole pairs of the VSM is 1.

(2) The primary frequency regulation of the VSM is ignored.

(3) The closed loop and its tracking are both neglected.

(4) The PV is considered to output constant power during the frequency changing process. The function of the ESS to suppress PV output active power is not considered in this paper. This is due to the fact that it may influence the volume margins of the ESS when the frequency changes.

A. Modelling of a VSM

An equivalent circuit and vector diagram of a VSM system are presented in Fig. 2. In Fig. 2(a), $\dot{E}$ is the potential of the VSM. $\dot{U}$ is the VSM terminal voltage. L is the equivalent inductance, R is the equivalent resistance, and $\dot{i}_g$ is the output current. In Fig. 2(b), ω is the angular frequency of $\dot{E}$. ω_g is the angular frequency of $\dot{U}$. δ is the power angle of the VSM, and α is the impedance angle.

Different VSM models can be built according to different synchronous machine (SM) models. A detailed model classification of VSMs is presented in [20]. This paper chooses a second-order model for analysis [22].

The swing equation of the VSM can be written as follows:

$$\begin{cases} 2H\dfrac{d\omega^*}{dt} = P_m^* - P_e^* - D(\omega^* - \omega_g^*) \\ \dfrac{d\delta}{dt} = \omega_0(\omega^* - \omega_g^*) \end{cases} \quad (1)$$

where P_m^* is the virtual shaft power determined by the governor, P_e^* is the measured output power, H is the virtual inertia constant, D is the virtual damping factor, ω_0 is the nominal angular frequency, and *suggests that the parameter is in per unit (p.u.).

The mathematical model of a VSM is built when there is a small variation on ω_g. The incremental model can be written as:

$$\begin{cases} 2H\dfrac{d\Delta\omega^*}{dt} = -\Delta P_e^* - D(\Delta\omega^* - \Delta\omega_g^*) \\ \dfrac{d\Delta\delta}{dt} = \omega_0(\Delta\omega^* - \Delta\omega_g^*) \end{cases} \quad (2)$$

Equ. (3) is obtained by applying a Laplace transform on Equ. (2), and it can be written as follows:

$$\begin{cases} 2Hs\Delta\omega^*(s) = -\Delta P_e^*(s) - D(\Delta\omega^*(s) - \Delta\omega_g^*(s)) \\ s\Delta\delta(s) = \omega_0(\Delta\omega^*(s) - \Delta\omega_g^*(s)) \end{cases} \quad (3)$$
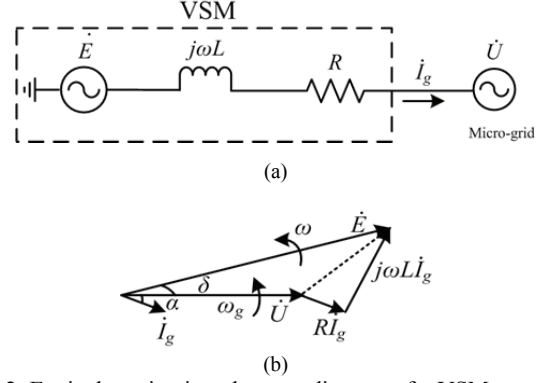

(a)

(b)

Fig. 2. Equivalent circuit and vector diagram of a VSM connected to a grid.

B. Relationship between the Output Active Power and Power Angle of a VSM

The output current of a VSM can be derived from Kirchhoff's law considering the equivalent resistance and inductance. Therefore:

$$\dot{I} = \frac{E\angle\delta - U}{Z\angle\alpha} \quad (4)$$

The output apparent power of the VSM can be conducted as follows:

$$\begin{aligned} S &= U\bar{I} \\ &= \frac{EU\angle(-\delta) - U^2}{Z\angle(-\alpha)} \\ &= \frac{EU}{Z}\cos(\alpha-\delta) + j\frac{EU}{Z}\sin(\alpha-\delta) - \frac{U^2}{Z}\cos\alpha - j\frac{U^2}{Z}\sin\alpha \\ &= P_e + jQ_e \end{aligned} \quad (5)$$

Where the superscript "-" indicates the conjugate operation of the element. The equivalent impedance $Z=((\omega L)^2+R^2)^{1/2}$, and the impedance angle $\alpha=\tan^{-1}(\omega L/R)$. P_e and Q_e can be acquired from Equ. (5) and written as:

$$\begin{cases} P_e = \dfrac{EU\cos(\alpha-\delta)}{Z} - \dfrac{U^2\cos\alpha}{Z} \\ Q_e = \dfrac{EU\sin(\alpha-\delta)}{Z} - \dfrac{U^2\sin\alpha}{Z} \end{cases} \quad (6)$$

The increment of the active power ΔP_e^* in Equ. (7) can be deduced from Equ. (6) and written as:

$$\Delta P_e^* = \frac{EU}{S_n Z}[\cos(\alpha-\delta-\Delta\delta) - \cos(\alpha-\delta)] \quad (7)$$

Considering that $\Delta\delta \to 0, \cos(\Delta\delta) \to 1, \sin(\Delta\delta) \to \Delta\delta$, Equ. (7) can be simplified as:

$$\Delta P_e^* \approx \frac{EU}{S_n Z}\sin(\alpha-\delta)\Delta\delta \quad (8)$$

Equ. (9) is obtained by applying a Laplace transform of Equ. (8) and it can be written as:

$$\Delta P_e^*(s) \approx \frac{EU}{S_n Z}\sin(\alpha-\delta)\Delta\delta(s) \quad (9)$$

Plug P_e=P_{ref} and Q_e=Q_{ref} into Equ. (6). P_{ref} is the reference of the output active power. Q_{ref} is the reference of the output reactive power. Therefore, E_s and δ_s can be calculated using Equ. (6).

$$\begin{cases} \delta_s = \alpha - \tan^{-1}(\dfrac{Q_{ref} + U^2 \sin\alpha / Z}{P_{ref} + U^2 \cos\alpha / Z}) \\ E_s = \dfrac{Q_{ref} Z + U^2 \sin\alpha}{U \sin(\alpha - \delta_s)} \end{cases} \quad (10)$$

where E_s is the potential of the VSM, and δ_s is the power angle at the steady state.

Let $S_E = EU\sin(\alpha-\delta)/(S_n Z)$, which is the synchronizing power coefficient. Equ. (11) can be obtained from Equ. (9) and Equ. (10).

$$S_E = Q_{ref}^* + \frac{U^2 \sin\alpha}{Z S_n} \quad (11)$$

where *suggests that the parameter is in per unit (p.u.). It shows that S_E is influenced by Q_{ref} instead of P_{ref} in Equ. (11).

C. Physical Constraints of a VSM

The transfer function of $\Delta\omega_g^*$ to ΔP_e^* can be deduced from Equ. (3) and Equ. (9), so that:

$$\frac{\Delta P_e^*(s)}{\Delta\omega_g^*(s)} = -\frac{2Hs\omega_0 S_E}{2Hs^2 + Ds + \omega_0 S_E} \quad (12)$$

The Laplace form of $\Delta\omega_g^*$ can be written as:

$$\Delta\omega_g^*(s) = \frac{\Delta\omega_g^*}{s} \quad (13)$$

According to Equ. (12) and Equ. (13), $\Delta P_e^*(s)$ can be written as:

$$\Delta P_e^*(s) = -\frac{2Hs\omega_0 S_E}{2Hs^2 + Ds + \omega_0 S_E}\frac{\Delta\omega_g^*}{s} \quad (14)$$

According to the poles' type of transfer function in (14), there are three different modes to be analyzed: under damping, over damping and critical damping. The maximum ΔP_e^* ($\Delta P_{e.max}^*$) can be deduced through an inverse Laplace transform for Equ. (14). $\Delta P_{e.max}^*$ is the peak value of the output active power variation, which means the employed ESS must have a power margin larger than $\Delta P_{e.max}^*$ to mimic the desired inertia characteristics. In addition, the energy constraint ΔE^* can be integrated from the shaded areas in Fig. 3.

1) Under Damping (Two Conjugate Complex Poles):

The dynamic response of the VSM output active power is shown in Fig. 3(a) when the grid frequency steps down.

ΔP_e^* can be obtained from an inverse Laplace transform on Equ. (14), and is written as:
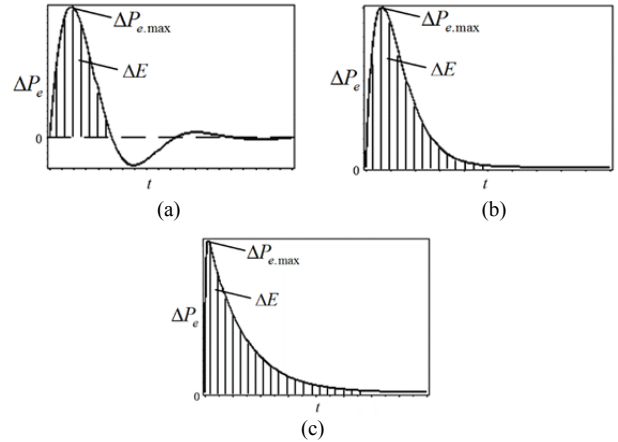

Fig. 3. Dynamic responses of the VSM output active power when the grid frequency steps down in three modes: (a) Under damping; (b) Over damping; (c) Critical damping.

$$\Delta P_e^*(t) = -\frac{4H\omega_0 S_E e^{-\frac{D}{4H}t}\Delta\omega_g^*}{m}\sin(\frac{m}{4H}t) \quad (15)$$

where m=$(8H\omega_0 S_E - D^2)^{1/2}$, and e is the Euler number.

When t=$4H\arctan(m/D)/m$, $\Delta P_{e.max}^*$ can be written as:

$$\Delta P_{e.max}^* = -\sqrt{2H\omega_0 S_E}\, e^{-\frac{D\arctan(m/D)}{m}}\Delta\omega_g^* \quad (16)$$

Let $\Delta P_e^*(t)$=0, and t=$4H\pi/m$ is the first zero point of $\Delta P_e^*(t)$ except for the original point. ΔE^* can be obtained from the integration of the shadow area in Fig. 3(a). Therefore:

$$\Delta E^* = \int_0^{4H\pi/m}(-\frac{4H\omega_0 S_E e^{-\frac{D}{4H}t}\Delta\omega_g^*}{m}\sin(\frac{m}{4H}t))\mathrm{dt}$$
$$= -2H(1 + e^{-\frac{\pi D}{m}})\Delta\omega_g^* \quad (17)$$

2) Over Damping (Two Unequal Negative Real Poles):

The dynamic response of the VSM output active power is shown in Fig. 3(b) when the grid frequency steps down. ΔP_e^* can be obtained from an inverse Laplace transform on Equ. (14), and is written as:

$$\Delta P_e^*(t) = -\frac{4H\omega_0 S_E e^{-\frac{D}{4H}t}\Delta\omega_g^*}{n}\sinh(\frac{n}{4H}t) \quad (18)$$

where n=$(D^2 - 8H\omega_0 S_E)^{1/2}$.

When t=$2H\ln[(D+n)/(D-n)]/n$, $\Delta P_{e.max}^*$ can be written as:

$$\Delta P_{e.max}^* = -\frac{8H\omega_0 S_E e^{-\frac{D\ln\frac{D+n}{D-n}}{n}}\sinh(0.5\ln(\frac{D+n}{D-n}))}{n}\Delta\omega_g^* \quad (19)$$

When $t \to \infty$, $\Delta P_e^* \to 0$. The integration time t is supposed to be $10H$ in order to simplify the expression of ΔE^*. ΔE^* can be obtained from the integration of the shadow area in Fig. 3(b) so that:

Mode	Power	Energy
under damping	Equ.(16)	Equ.(17)
over damping	Equ.(19)	Equ.(20)
critical damping	Equ.(22)	Equ.(23)

TABLE II
PARAMETERS OF A VSM

Parameter	Value	Parameter	Value
S_n	250kVA	P_{ref}	10kW
U_g(L-L)	380V	U_{dc}	800V
L	1.5mH	ω_{ref}	314rad/s
R	0.2Ω	$\Delta\omega_g^*$	0.01

$$\Delta E^* = \int_0^{10H} (-\frac{4H\omega_0 S_E e^{-\frac{D}{4H}t}\Delta\omega_g^*}{n}\sinh(\frac{n}{4H}t))dt \quad (20)$$

$$= \frac{H}{n}\left[(n+D)e^{\frac{5(n-D)}{2}} + (n-D)e^{-\frac{5(n+D)}{2}} - 2n\right]\Delta\omega_g^*$$

3) Critical Damping (Two Equal Negative Real Poles):

The dynamic response of the VSM output active power is shown in Fig. 3(c) when the grid frequency steps down.

ΔP_e^* can be obtained from an inverse Laplace transform on Equ. (14) and is written as:

$$\Delta P_e^*(t) = -\omega_0 S_E t e^{-\frac{D}{4H}t}\Delta\omega_g^* \quad (21)$$

When $t=4H/D$, $\Delta P_{e.max}^*$ can be written as:

$$\Delta P_{e.max}^* = -\frac{4H\omega_0 S_E}{De}\Delta\omega_g^* \quad (22)$$

When $t \to \infty$, $\Delta P_e^* \to 0$. The integration time t is infinite. ΔE^* can be obtained from an integration of the shadow area in Fig. 3(c) so that:

$$\Delta E^* = \int_0^\infty (-\omega_0 S_E t e^{-\frac{D}{4H}t}\Delta\omega_g^*)dt = -\frac{16H^2\omega_0 S_E}{D^2}\Delta\omega_g^* \quad (23)$$

According to Table I, the relationships between the power and energy margins, inertia constant H, damping factor D and reference of the reactive power Q_{ref} are revealed. Once the power and energy volume of the ESS equipment are fixed, the possible inertia and damping characteristics that the VSM can mimic are restricted. Those are the proposed physical constraints of the energy storage based VSM.

III. PARAMETER INFLUENCES ON THE DYNAMIC BEHAVIORS OF VSMS

In this section, the influences of H, D and Q_{ref} on VSM dynamic behaviors are analyzed. Bode diagrams and pole trajectories are presented. The physical constraints on H, D and Q_{ref} are further studied theoretically. The parameters of the system are shown in Table II. When Q_{ref}=0kVar and H=0.05s, S_E can be calculated as 1.038. In addition, D=11.42 is calculated for the critical damping mode.

A. Influences of H, D and Q_{ref} on VSM Dynamic Behaviors

The operating points are set at P_{ref}=10kW and Q_{ref}=0kVar. The control parameters are set at H=0.05s and D=11.42 when

Q_{ref} changes. The Bode diagrams in Fig. 4 are obtained from Equ. (12).

According to the amplitude-frequency characteristics in Fig. 4(a) and (d), H influences the low frequency band characteristics. The phase-frequency characteristics reveal that a larger H makes a smaller phase margin. In addition, the effect of H on the phase margin is mainly distributed on the middle frequency band.

The amplitude-frequency characteristics and phase-frequency characteristics in Fig. 4 (b) and (e) show that D only influences the middle frequency band characteristics. In addition, D has little effect on the magnitude-frequency characteristic. A larger D makes a lager phase margin.

Fig. 4(c) and (f) show that Q_{ref} influences the amplitude-frequency characteristic in the high frequency band and the phase-frequency characteristic in the low frequency band. An increase of Q_{ref} results in an increase of the phase margin.

The pole trajectories got from Equ. (14) are presented in Fig. 5. The radical lines indicate the damping ratio and the circle lines indicate the nature frequency.

In Fig. 5(a), the poles are distributed on the negative real axis when D varies from 14 to 18. In addition, the VSM operates in the over damping mode. The poles are conjugate complex when D varies from 5 to 9. In addition, the VSM operates in the under damping mode. It indicates that the system tends to be stable when D increases.

In Fig. 5(b), the poles are distributed on the negative real axis when H varies from 0.02s to 0.04s. In addition, the VSM operates in the over damping mode. The poles are conjugate complex when H varies from 0.1s to 0.2s. In addition, the VSM operates in the under damping mode. This indicates that the system tends to oscillate less when H decreases.

In Fig. 5(c), the poles are distributed on the negative real axis when Q_{ref} varies from -10kVar to -30kVar. In addition, the VSM operates in the over damping mode. The poles are conjugate complex when Q_{ref} varies from 10kVar to 30kVar. In addition, VSM operates in the under damping mode. This indicates that the system tends to be stable when Q_{ref} decreases.

The dynamic responses of the output active power when the grid frequency steps down by 1% are shown in Fig. 6. These results show that H, D and Q_{ref} are all related to the power and energy margins. The influences of the three factors on the power and energy margins are shown in Fig. 7. The
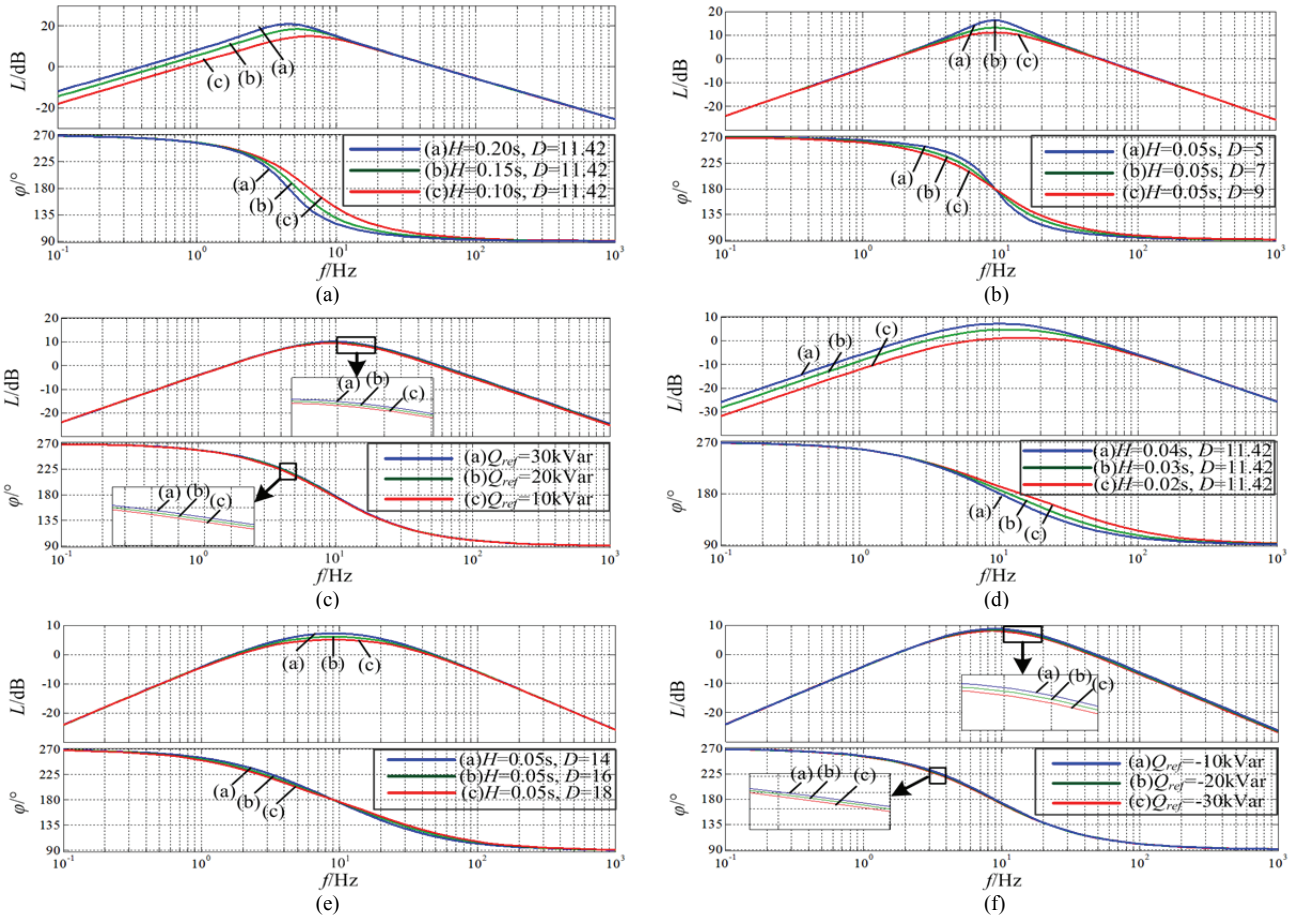
Fig. 4. Bode diagrams; (a) Under damping with different H. (b) Under damping with different D, (c) Under damping with different Q_{ref}, (d) Over damping with different H, (e) Over damping with different D, (f) Over damping with different Q_{ref}.
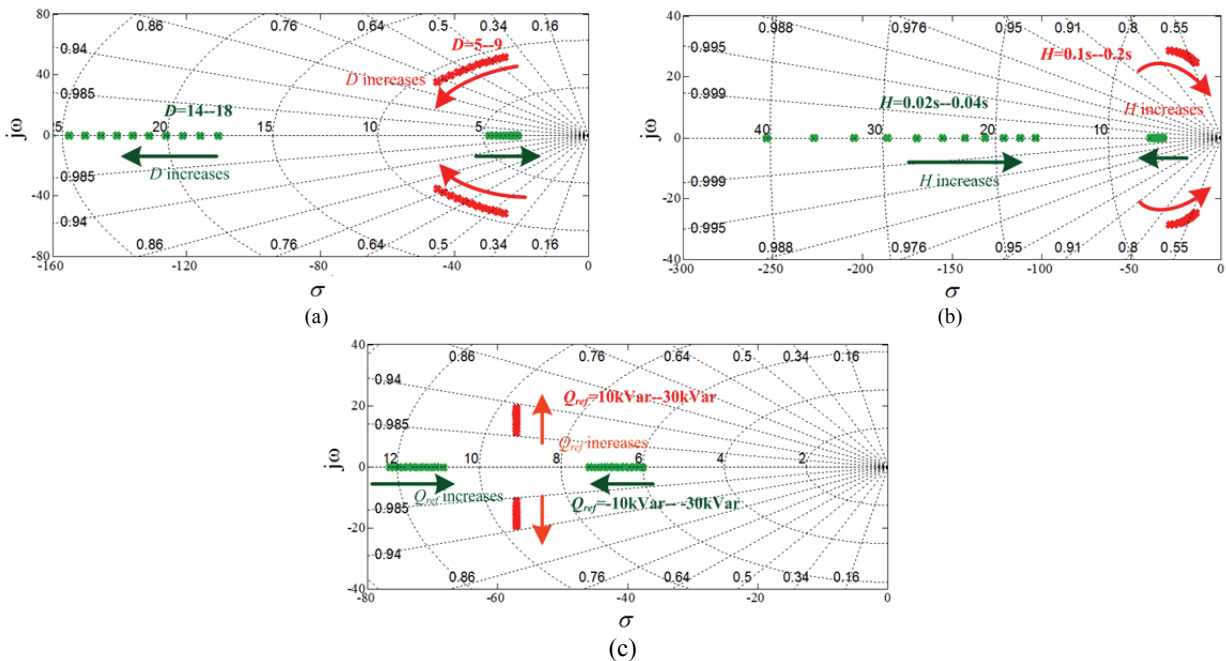

Fig. 5. Poles trajectories. (a) D varies from 5 to 9 and from 14 to 18 when H=0.05s, Q_{ref}=0kVar. (b) H varies from 0.02s to 0.04s and from 0.1s to 0.2s when D=11.42, Q_{ref}=0kVar. (c) Q_{ref} varies from -30kVar to -10kVar and from 10kVar to 30kVar when H=0.05s, D=11.42.
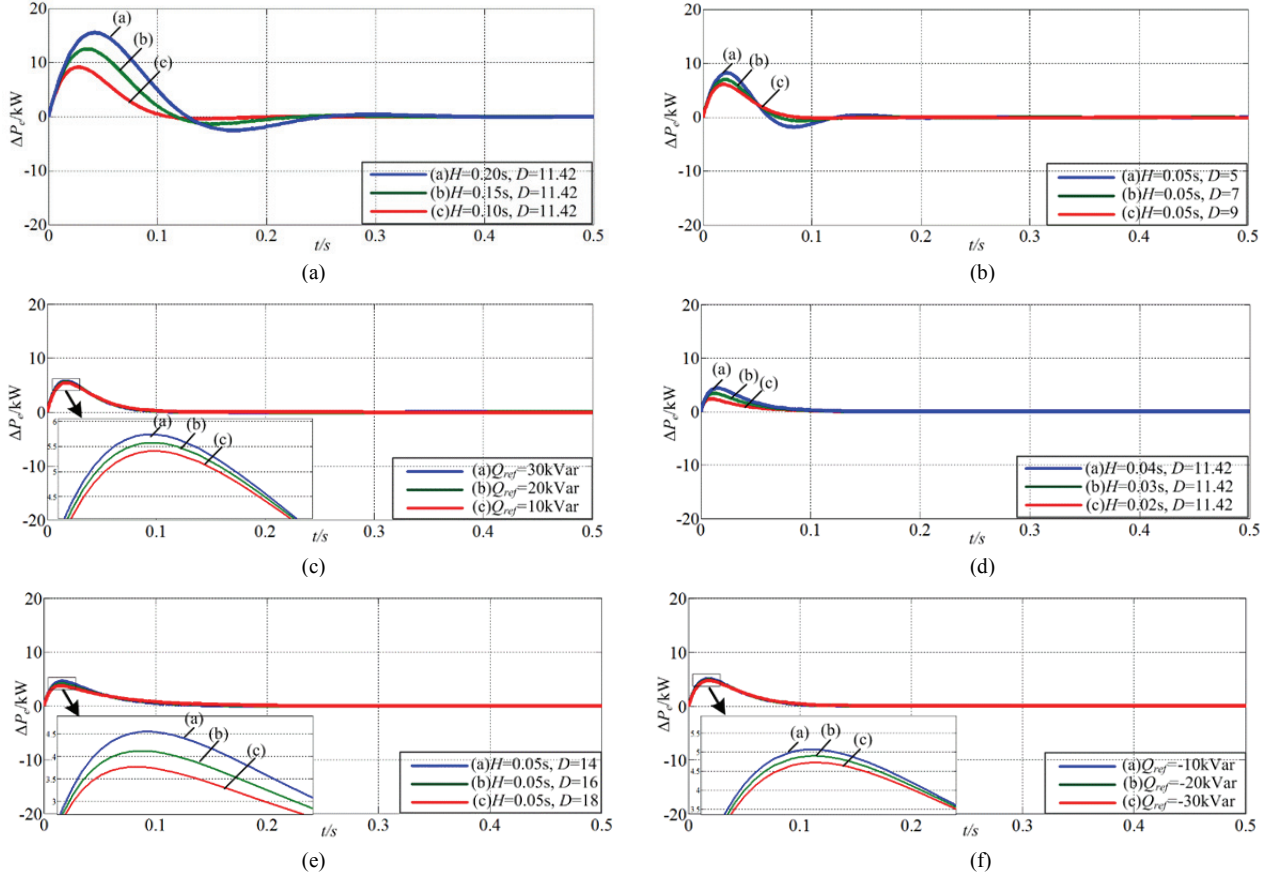
Fig. 6. Theoretic dynamic responses of the output active power when the grid frequency steps down by 1%. (a) Under damping with different values of H when Q_{ref}=0kVar, D=11.42. (b) Under damping with different values of D when Q_{ref}=0kVar, H=0.05s. (c) Under damping with different values of Q_{ref} when H=0.05s, D=11.42. (d) Over damping with different values of H when Q_{ref}=0kVar, D=11.42. (e) Over damping with different values of D when Q_{ref}=0kVar, H=0.05s. (f) Over damping with different values of Q_{ref} when H=0.05s, D=11.42.

power and energy margins should increase when H increases and D decreases as shown in Fig. 7(a) and (c). However, the energy margins do not change when D increases to a certain extent as shown in Fig. 7(d). An increase of Q_{ref} makes the power margin increase in Fig. 7(e). However, Q_{ref} has a slight effect on the energy margin as shown in Fig. 7(f).

$$E_k = \frac{1}{2} J \omega_0^2 \qquad (24)$$

where J is the virtual inertia, and E_k is the kinetic energy stored in the rotor. H varies between 2s and 10s for a typical SM although it depends on the machine size and power [9]. However, the setting of the VSM inertia constant can be more flexible than the SM.

$$H = \frac{E_k}{S_n} = \frac{1}{2} \frac{J \omega_0^2}{S_n} \qquad (25)$$

E_k and H can be defined by Equ. (24) and Equ. (25), respectively [23]. The energy E_k increases while H increases according to Equ. (25). The damping factor D possesses the function for damping power fluctuations. Therefore, $\Delta P_{e.max}^*$

and ΔE^* decrease when D increases. It can also be concluded from Fig. 6 that H is related to the oscillation frequency and D is related to the speed of the oscillation attenuation.

B. Physical Constraints on H, D and Q_ref

It is preferable for the VSM to operate on the over damping mode in order to relieve frequency transitions and to avoid a large overshoot. Therefore, this paper chooses the over damping mode when H varies from 0 to 1s and D varies from 54 to 100. Fig. 8 illustrates the relationships among power and energy margins, H, D and Q_{ref}.

Power margin surfaces with different values of Q_{ref}^* and 10kW power constraint surface are shown in Fig. 8(a). It can be seen that an increase of Q_{ref}^* raises the power margin. Projections of $\Delta P_{e.max}$ and $\Delta P_{e.max}$ =10kW when Q_{ref}^*=0 are presented in Fig. 8(b). The intersecting line divides the projection into two parts. The parameters under and beyond the physical constraint fall within area I and area II, respectively.

Energy margin surfaces with different values of Q_{ref}^* and energy constraint surface are shown in Fig. 8(c). It can be
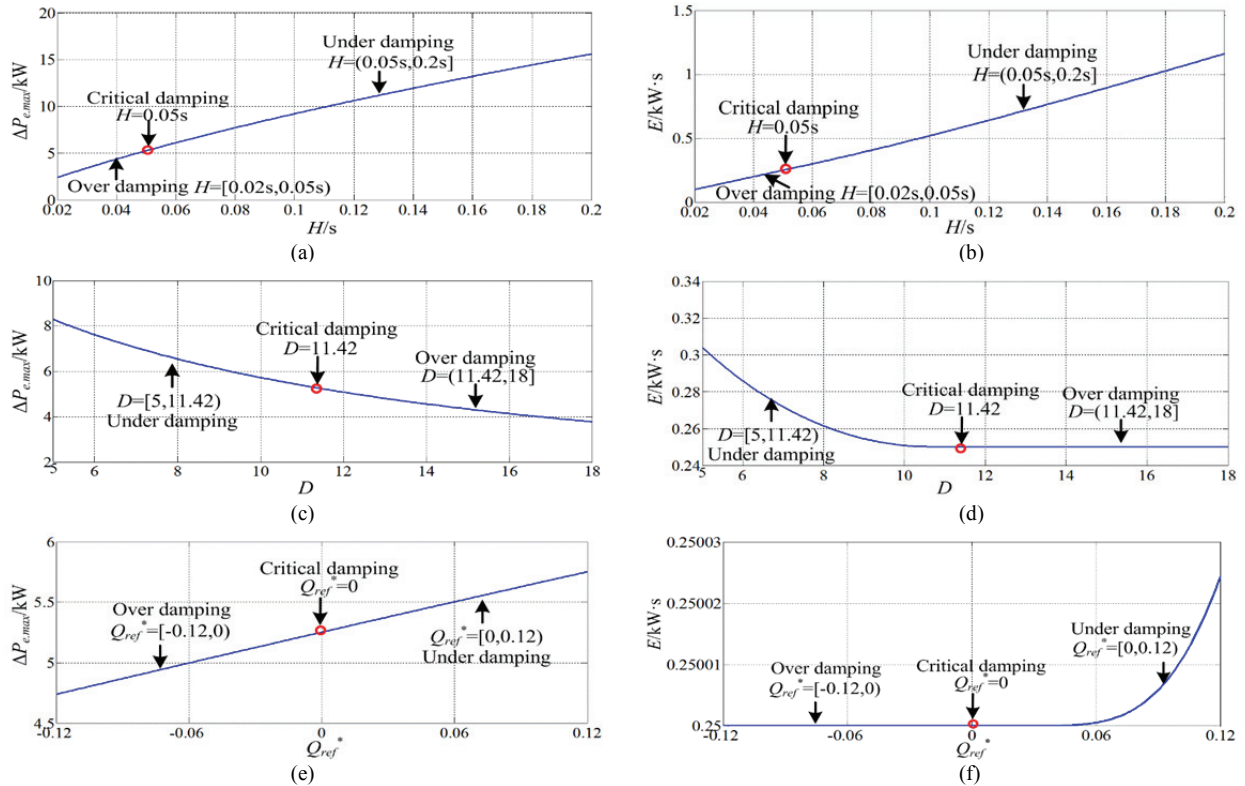
Fig. 7. Piecewise curves of power and energy margins. (a) H varies from 0.02s to 0.2s when D=11.42, Q_{ref}=0kVar. (b) H varies from 0.02s to 0.2s when D=11.42, Q_{ref}=0kVar. (c) D varies from 5 to 18 when H=0.05s, Q_{ref}=0kVar. (d) D varies from 5 to 18 when H=0.05s, Q_{ref}=0kVar. (e) Q_{ref}^* varies from -0.12 to 0.12 when H=0.05s, D=11.42. (f) Q_{ref}^* varies from -0.12 to 0.12 when H=0.05s, D=11.42.
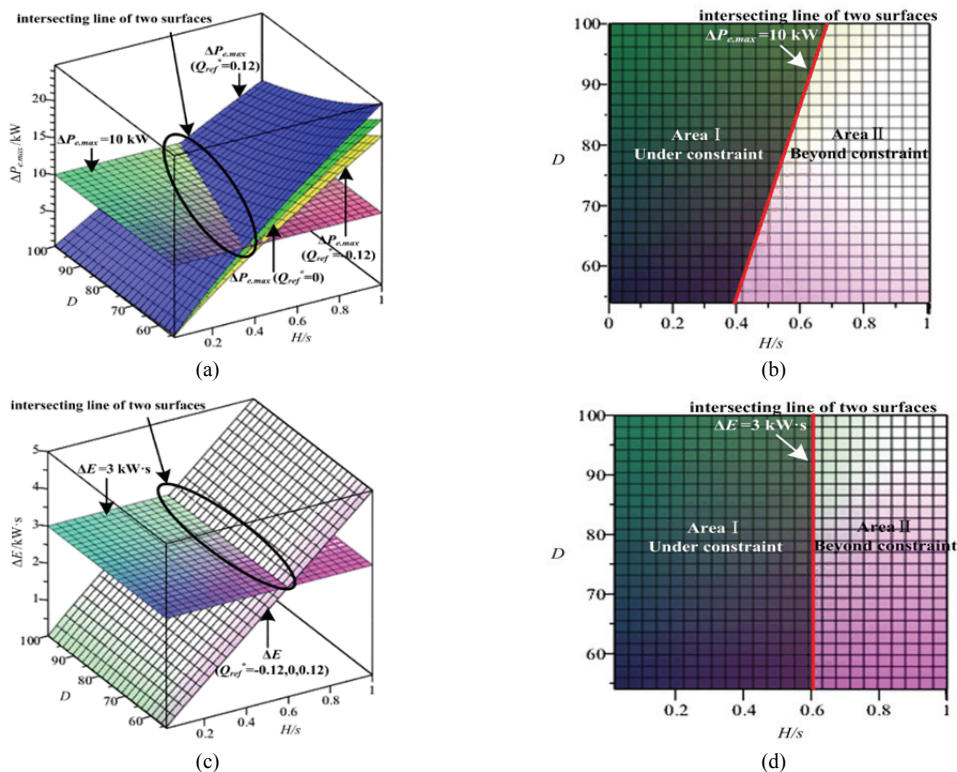

Fig. 8. Power and energy margins with physical constraints. (a) Power margin surfaces and power constraint surface. (b) Projection of subgraph a when Q_{ref}^*=0 on bottom surface. (c) Energy margin surfaces and energy constraint surface. (d) Projection of subgraph c when Q_{ref}^*=0 on bottom surface.
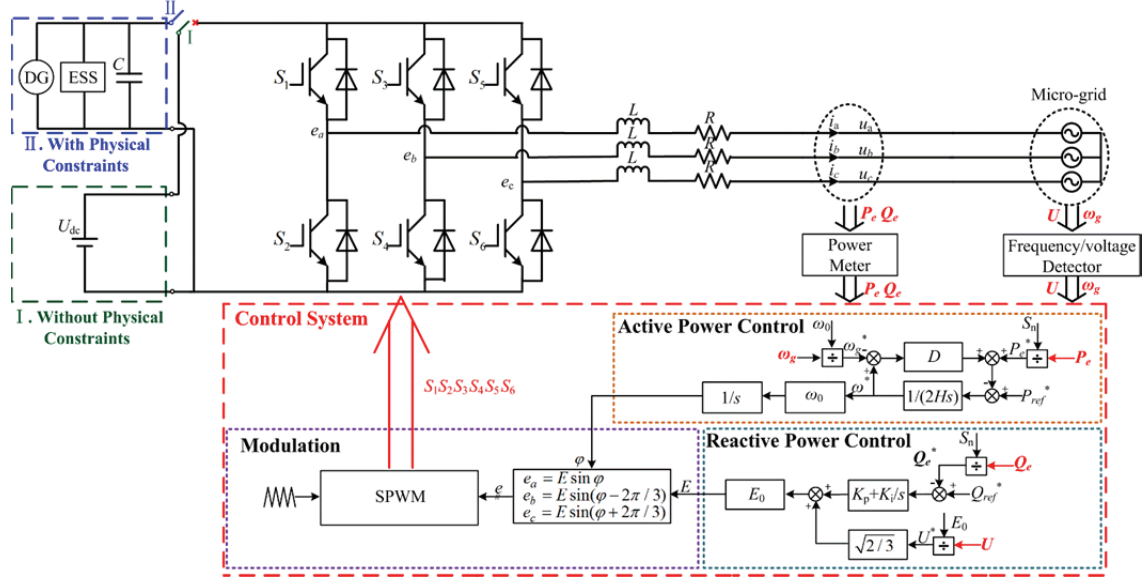
Fig. 9. System configuration and control diagram.

seen that an increase of Q_{ref}^* has little effect on the energy margin. Projections of ΔE and ΔE=3 kW·s when Q_{ref}^*=0 are presented in Fig. 8(d). The intersecting line divides the projection into two parts. The parameters under and beyond the physical constraint fall within area I and area II, respectively.

IV. SIMULATION RESULTS

PSCAD/EMTDC® is a widely accepted simulation tool, especially in electrical power systems. PSCAD/EMTDC includes a comprehensive library of system models ranging from simple passive elements and control functions, to electric machines and other complex devices. In addition, PSCAD has become the graphical user interface of RTDS.

In this section, the simulation system configuration and control system are presented first. The simulations are carried out when the frequency steps up and down to verify the theoretical analysis. In addition, simulations when the power constraints are broken are also studied in detail. The parameters of the VSM simulation system are the same as those of the theoretical analysis in Table II. The simulations are carried out in PSCAD/EMTDC, without smoothing in order to be consistent with the theoretical analysis results. The switching frequency is set at 10 kHz and the solution time step is set to 1μs.

A. Simulation System Configuration and Control Diagram

The simulation system configuration and the control diagram of a VSM are presented in Fig. 9.

The active power control is designed according to Equ. (1). The primary frequency regulation is ignored. The rotor angle φ can be written as:

$$\varphi = \omega_0 \int \{[P_{ref}^* - P_e^* - D(\omega^* - \omega_g^*)] / 2H\} dt \qquad (26)$$

The reactive power control is achieved by changing the internal potential amplitude E of the VSM. The internal potential amplitude E can be written as:

$$E = [(Q_{ref}^* - Q_e^*)(K_p + K_i / s) + \sqrt{2/3}U^*]E_0 \qquad (27)$$

where K_p is the coefficient of proportionality, and K_i is integral coefficient.

The DC side of the VSM is divided into two modes. The DC side in mode I is a voltage source at 800V. The DC side in mode II is a voltage source initially. However, it is switched to a constant power source when the physical constraints are broken. The simulations in 4.2 and 4.3 are carried out in mode I, and the simulations in 4.4 are carried out in mode II.

B. Dynamic Responses of the Output Active Power when P_{ref} Steps

The simulation results in Fig. 10 indicate that the VSM can realize the inertia and damping characteristics well. The simulations start at t=0. Initially, P_{ref} is set at 10kW, and Q_{ref} is set at 0kVar. 30kW is applied to P_{ref} at t=1.0s, and 10kW is then applied to P_{ref} at t=3.0s. In Fig. 10(c) and (d), the under damping mode causes a larger overshoot when compared with the over damping mode in Fig. 10(a) and (b). According to the simulation results, the VSM system can provide inertia and damping well with different values of H and D.

C. Dynamic Responses of the Output Active Power when the Grid Frequency Steps by 1%

The dynamic responses of the active power with different values of H and D when the grid frequency steps by 1% are
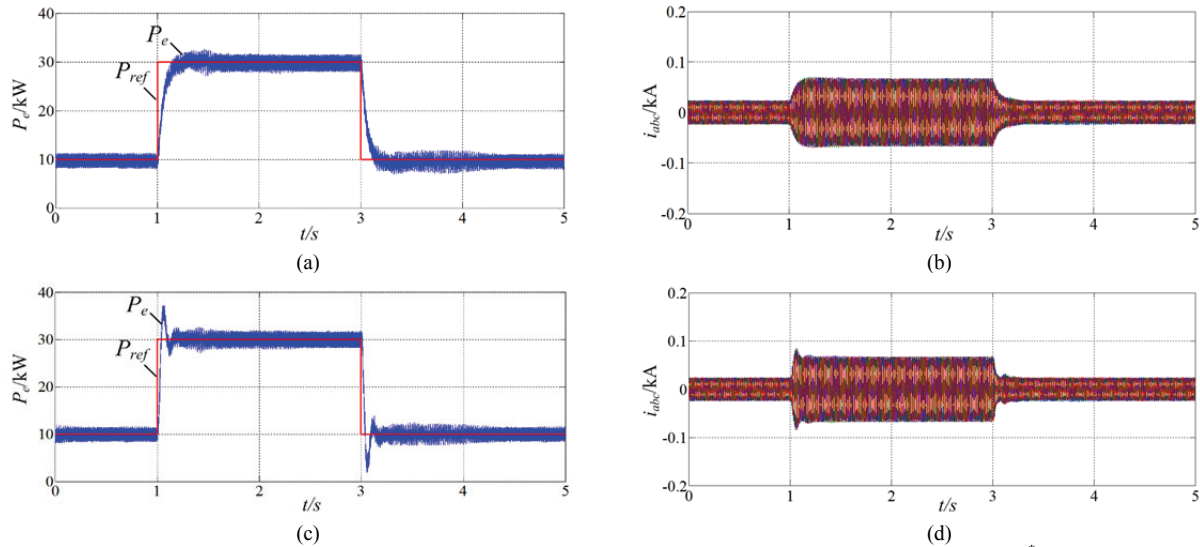
Fig. 10. Dynamic responses of the output active power and currents when P_{ref} steps. (a) H=0.05s, D=20, Q_{ref}^*=0 (over damping). (b) Three phases currents (over damping). (c) H=0.05s, D=5, Q_{ref}^*=0 (under damping). (d) Three phases currents (under damping).
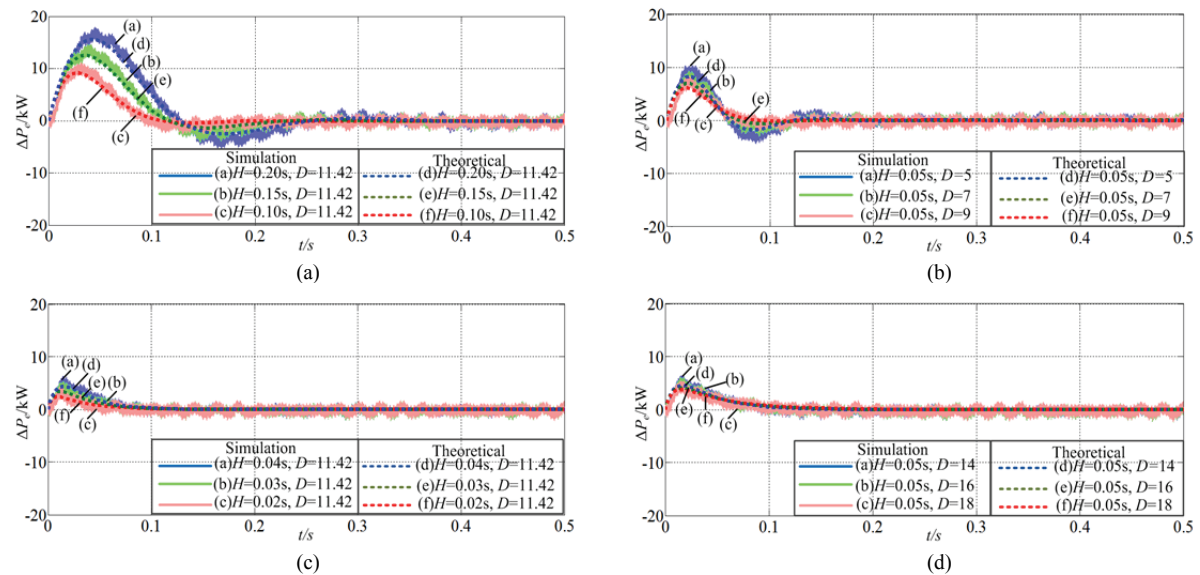

Fig. 11. Dynamic responses of the output active power ΔP_e when the grid frequency steps down by 1%. (a) Under damping with different values of H. (b) Under damping with different values of D. (c) Over damping with different values of H. (d) Over damping with different values of D.

shown in Fig. 11 and Fig. 12. The simulations in Fig. 11 and Fig. 12 are carried out when P_{ref}=10kW and Q_{ref}=0kVar in the steady state. The grid frequency steps at t=0s after the initial process which is ignored.

The simulation results are consistent with the theoretical analysis results. The theoretical analysis results and simulation data are presented in Table III. The power and energy margins increase when H increases and D decreases. However, the energy margins do not change when the damping factor D increases to a certain extent.

The simulations in Fig. 13 and Fig. 14 are carried out when H=0.05s and D=11.42. P_{ref} is set at 10kW when Q_{ref} changes as shown in Fig. 13(a)-(c) and Fig. 14(a)-(c). Q_{ref} is set at

0kVar when P_{ref} changes as shown in Fig. 13(e) and Fig. 14(e). The grid frequency steps by 1% at t=0s after the initial process. The data of the power and energy margins in Fig. 13 are presented in Table III.

According to Fig. 13(a) and Fig. 14(a), the power margin increases when the VSM outputs more inductive reactive power. However, Q_{ref} has a slight effect on the energy margin. The output currents and voltage of phase A when Q_{ref}=30kVar are presented in Fig. 13(b) and Fig. 14(b). The voltage of phase A is ahead of the current. Thus, the VSM outputs inductive reactive power.

According to Fig. 13(c) and Fig. 14(c), the power margin decreases when the VSM outputs more capacitive reactive
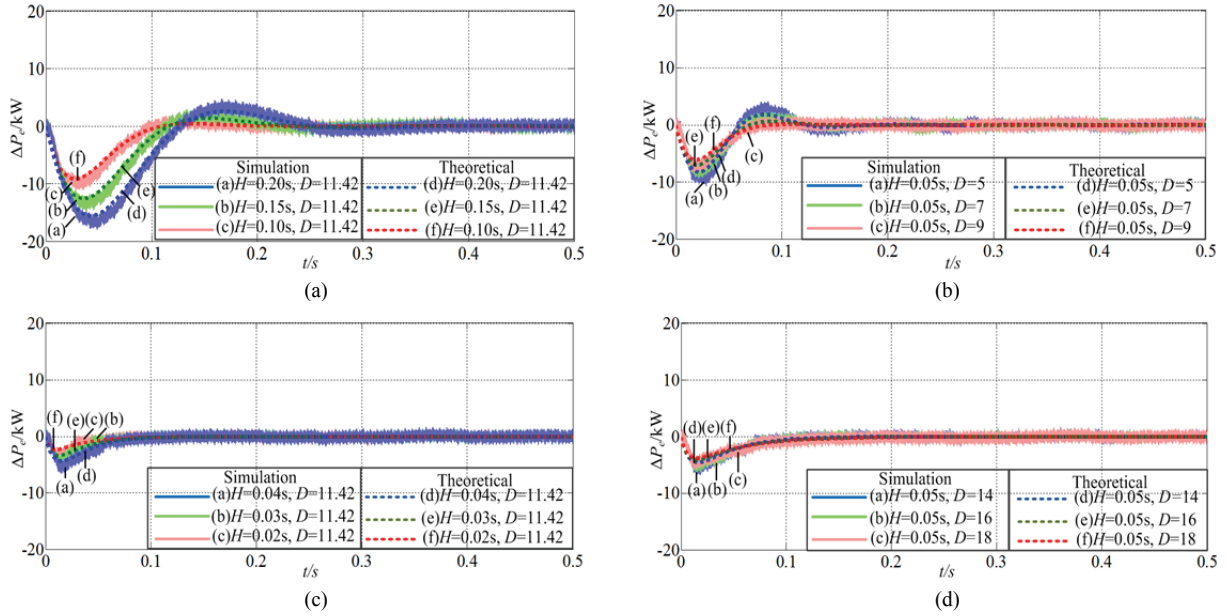
Fig. 12. Dynamic responses of the output active power ΔP_e when the grid frequency steps up by 1%. (a) Under damping with different values of H. (b) Under damping with different values of D. (c) Over damping with different values of H. (d) Over damping with different values of D.
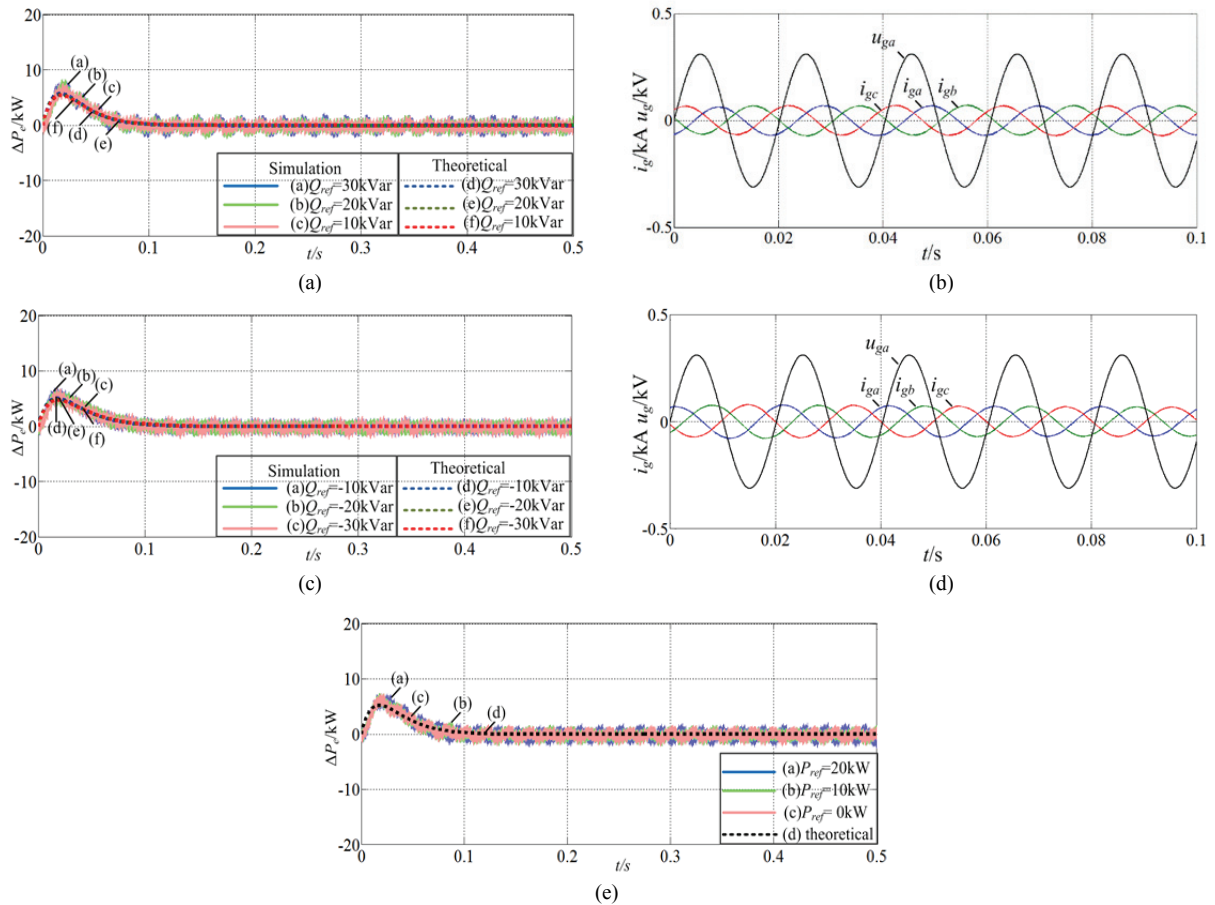

Fig. 13. Dynamic responses of the output active power ΔP_e when the grid frequency steps down by 1%. (a) Under damping with different values of Q_{ref}. (b) Output currents and voltage when Q_{ref}=30kVar. (c) over damping with different Q_{ref}. (d) output current and voltage when Q_{ref}=-30kVar. (e) Critical damping with different values of P_{ref}.
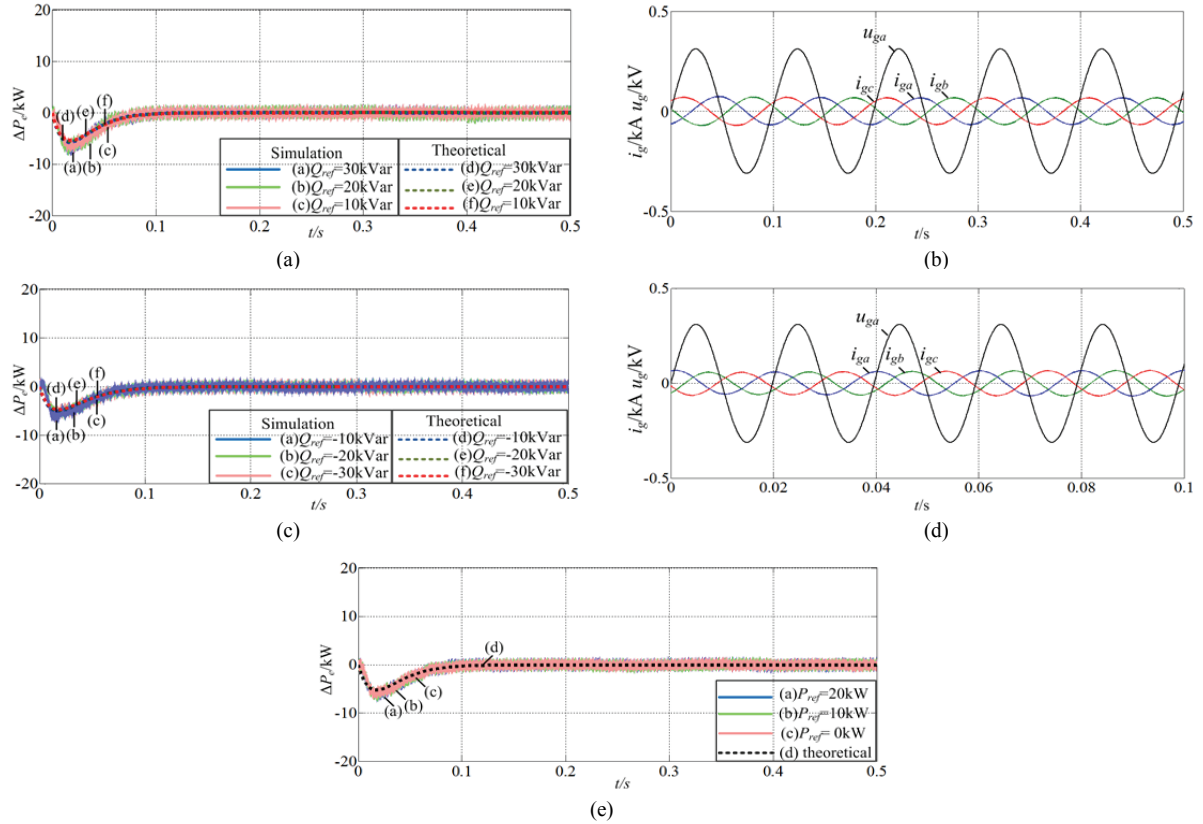
Fig. 14. Dynamic responses of the output active power ΔP_e when the grid frequency steps up by 1%. (a) Under damping with different values of Q_{ref}. (b) Output current and voltage when Q_{ref}=30kVar. (c) Over damping with different values of Q_{ref}. (d) Output current and voltage when Q_{ref}=-30kVar. (e) Critical damping with different values of P_{ref}.

TABLE III
COMPARISON OF THE THEORETICAL RESULTS AND SIMULATIONS OF POWER AND ENERGY MARGINS

Mode	Fixed parameter	Variable parameter	Power margin(kW)			Energy margin(kW·s)		
			Theoretical (kW)	Simulation (kW)	Error (%)	Theoretical (kW·s)	Simulation (kW·s)	Error (%)
Under damping	D=11.42, Q_{ref}=0	H=0.10s	9.1848	9.6643	5.22	0.5216	0.5364	2.84
		H=0.15s	12.5562	13.3522	6.34	0.8314	0.8651	4.05
		H=0.20s	15.5652	16.4530	5.70	1.1604	1.2060	3.93
	H=0.05s, Q_{ref}=0	D=5	8.2670	8.7672	6.05	0.3041	0.3255	7.04
		D=7	7.0263	7.2780	3.58	0.2719	0.2828	4.01
		D=9	6.0944	6.3356	3.96	0.2545	0.2585	1.57
	H=0.05, D=11.42	Q_{ref}^{*}=0.12	5.7389	5.7320	-0.12	0.2500	0.2510	0.40
		Q_{ref}^{*}=0.08	5.5739	5.8263	4.53	0.2500	0.2520	0.80
		Q_{ref}^{*}=0.04	5.4075	5.4608	0.99	0.2500	0.2515	0.60
Over damping	D=11.42, Q_{ref}=0	H=0.02s	2.3773	2.1506	-9.54	0.0998	0.0983	-1.50
		H=0.03s	3.3939	3.2933	-2.96	0.1500	0.1492	-0.53
		H=0.04s	4.3432	4.3432	-0.77	0.2000	0.1998	-0.10
	H=0.05s, Q_{ref}=0	D=14	4.5492	4.6350	1.89	0.2500	0.2471	-1.16
		D=16	4.1233	4.1739	1.23	0.2500	0.2489	-0.44
		D=18	3.7682	3.8073	1.04	0.2500	0.2462	-1.52
	H=0.05, D=11.42	Q_{ref}^{*}=-0.12	4.7257	4.7489	0.49	0.2500	0.2418	-3.28
		Q_{ref}^{*}=-0.08	4.8985	4.9481	1.01	0.2500	0.2468	-1.28
		Q_{ref}^{*}=-0.04	5.0699	5.0980	0.55	0.2500	0.2462	-1.52
Different active power	H=0.05, D=11.42, Q_{ref}=0	P_{ref}=20kW	5.2524	5.6020	6.66	0.2499	0.2570	2.84
		P_{ref}=10kW	5.2524	5.4165	3.12	0.2499	0.2507	0.32
		P_{ref}=0kW	5.2524	5.3559	1.97	0.2499	0.2406	0.28

power. However, Q_{ref} has a slight effect on the energy margin. The output currents and voltage of phase A when Q_{ref}=-30kVar are presented in Fig. 13(d) and Fig. 14(d). The voltage of phase A lags behind the current. Thus, the VSM outputs capacitive reactive power.

The simulations in Fig. 13(e) and Fig. 14(e) are carried out with different values of P_{ref} when the VSM operates in the unity-power factor mode. It can be concluded that P_{ref} has no effect on the power and energy margins.

Based on the analysis above, changes of the reactive power influence the power and energy margins. An increase of the inductive reactive power makes the power margin increase and it has a slight effect on the energy margin. The output active power in the steady state has no effect on the power and energy margins.

Using grid frequency steps down as an example, the theoretical analysis results and simulation data in Fig. 11 and Fig. 13 are listed in Table III. These simulation values are obtained after filtering. A second-order Butterworth filter with a cut-off frequency of 20Hz is used. Errors are calculated by error = (simulation-theoretical)/ theoretical* 100%. The errors in Table III are all less than 10%. Thus, the theoretical analysis is verified by simulations.

D. Behaviors of a VSM when the Physical Constraints are Broken

The DC side in this part is in mode II. It is a dc voltage source with a small internal resistance at the beginning. In addition, it switches to the constant power mode when the VSM reaches its power constraint. A 2000uF capacitor is connected with the source in parallel. According to Fig. 8(b), the parameters under and beyond the physical constraints can be set to H=0.2s, D=60 and H=0.7s, D=60. In addition, P_{ref}=10kW and Q_{ref}=0kVar are set as the steady state. The grid frequency steps down by 1% at t=0s after the initial process in Fig. 15. The theoretical analysis results and simulations are presented without physical constraints. $\Delta P_{e.max}$ in Fig. 15(a) is 6.5228kW, and $\Delta P_{e.max}$ in Fig. 15(b) is 15.4422kW. If the power constraint is set at 10kW, the VSM operates with H=0.7s, and D=60 breaks the power constraint.

The simulation results are shown in Fig. 16 when the VSM operates with H=0.7s, D=60, Q_{ref} =0kVar and P_{ref} =10kW. The power constraint is set at 10kW, and the grid frequency steps down at t=0s. The VSM operates normally to output more active power to support the grid frequency when t=0~t_1. The output active power of the VSM reaches the power constraint at t=t_1. Meanwhile, the DC capacitor voltage is starting to decrease in Fig. 16(a) after t=t_1. The relays act when the direct voltage decreases by 20% of the rated voltage. Then the whole VSM system is shut down (Fig. 16(b) and (c)). The DC capacitor voltage remains unchanged. The output active power and currents decrease to zero.
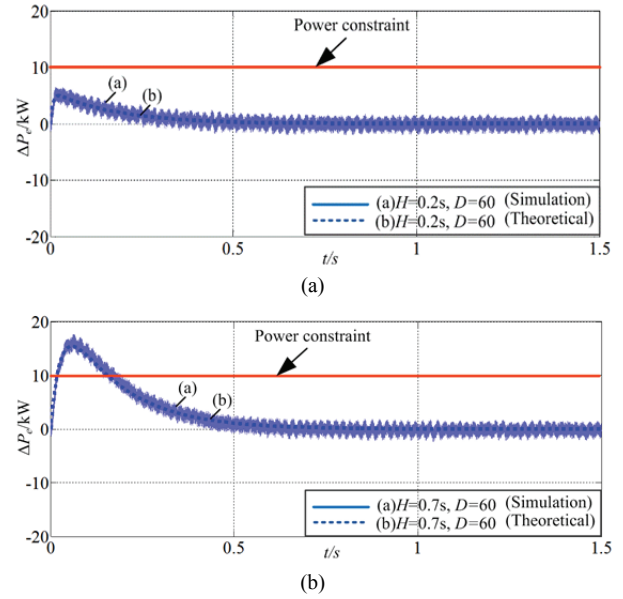

Fig. 15. Dynamic responses of the output active power ΔP_e when the grid frequency steps down by 1%. (a) H=0.2s, D=60, Q_{ref}^*=0 (parameters under physical constraints). (b) H=0.7s, D=60, Q_{ref}^*=0 (parameters beyond physical constraints).
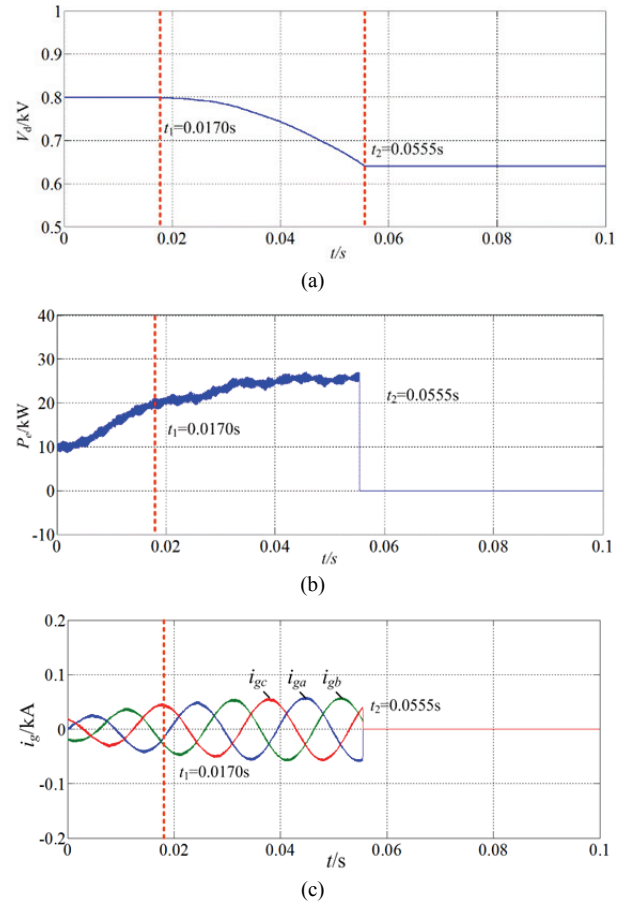

Fig. 16. Behaviors of the VSM when the physical constraints are broken. (a) DC voltage V_d. (b) Output active power P_e. (c) Output current i_g.
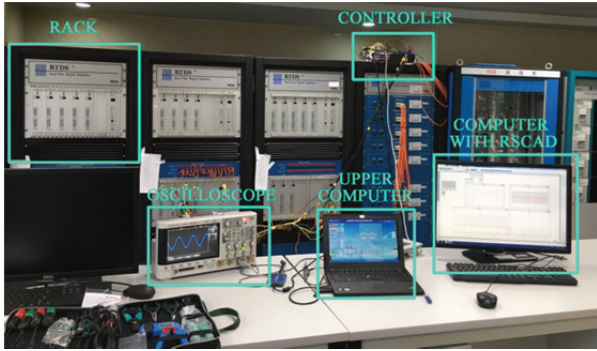
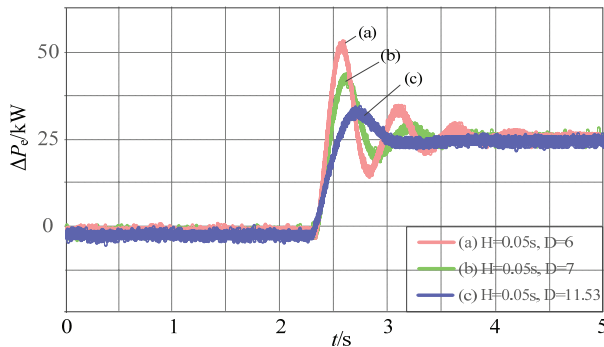Fig. 17. Photo of the RTDS experiment system.

Fig. 18. Dynamic responses of the output active power when P_{ref} steps with different values of D.
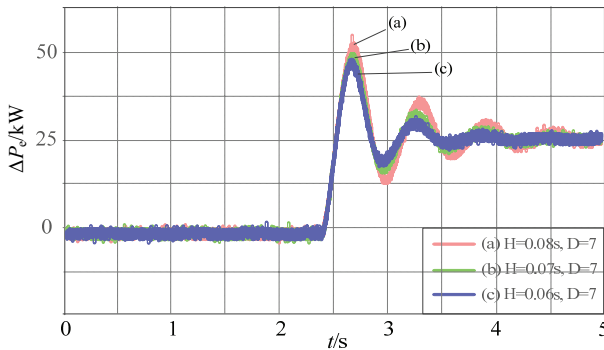

Fig. 19. Dynamic responses of the output active power when P_{ref} steps with different values of H.

V. RTDS EXPERIMENTAL RESULTS

Real-Time Digital Simulator (RTDS) is a supercomputer designed to test the electromagnetic transients in electric power systems. It was developed by the Manitoba HVDC Research Center, Winnipeg, Canada, in 1994. The RTDS is comprised of a RSCAD workstation and racks. Each rack has multiple plug-in processing cards and communication plug-in components. With its powerful parallel processing capacity, the RTDS can simulate a large power networks in real-time for analyzing electromagnetic transients.

In this paper, a VSM experiment system is built completely on RTDS. The employed rack has 12 GPC and 3GP cards, and each GPC or 3GP card has 2 processors. Fig. 17 shows

the entire experiment setup of the RTDS system. The VSM model is built in RSCAD, and the computer with RSCAD are connected to the rack through a cable. The physical control box linked to the upper computer is directly connected with the rack. Experimental results can be displayed on the oscilloscope which is connected through the Analogue Output Card.

The system configuration and a control diagram of the VSM are presented in Fig. 9. The parameters of the VSM experimental system are same as those of the theoretical analysis. Experiments start at P_{ref} =0kW and Q_{ref} =5kVar. (When Q_{ref}=5kVar and H=0.05s, D can be calculated as 11.53 for the critical damping mode). Seconds after the system is stable, 25kW is applied to P_{ref}. The dynamic responses of the output active power are presented when P_{ref} steps with different values of H and D. Fig.18 shows the dynamic responses of the output active power when H=0.05 and D=6, 7, 11.53. When D increases, the peak value of the output active power reduces and the amplitude quickly decreases. Fig.19 shows the dynamic responses of the output active power when D=7 and H=0.08, 0.07, 0.06. When H increases, the peak value of the output active power increases and the characteristic of the inertia is more noticeable. In general, the peak value of the output power should increase when H increases or when D decreases. The results of the RTDS experiment agree with the theoretical analysis.

VI. CONCLUSIONS

In this paper, VSM physical constraints are proposed. The influences of key parameters and operating points on the physical constraints are quantitatively analyzed in detail. Bode diagrams and poles trajectories verify these analysis. The transient characteristics and physical constraints of a grid-tie VSM are studied. Finally, the theoretical analysis is verified by simulation and experimental results. The main conclusions are summarized as follows.

(1) Transient characteristics are investigated and physical constraints are proposed based the VSM in this paper. The analytic solutions in Table I are deduced through a theoretical analysis. The inertia constant H, damping factor D and operating point of the reactive power Q_{ref} are all related to the power and energy margins.

(2) The influences of H, D and Q_{ref} on the physical constraints are investigated by quantitative analysis and simulations. The power and energy margins should increase when H increases and D decreases. Q_{ref} has an effect on the power margin and a slight effect on the energy margin. P_{ref} has no effect on the power or energy margins.

(3) The physical constraints and parameters setting ranges are discussed in detail. Parameters beyond the physical constraints cause a sudden decrease of the DC voltage and the whole VSM system is shut down.

The results and analysis in this paper provide a useful basis for the further investigation of VSM transient characteristics. In addition, the physical constraints propose a clear parameters setting principle of the VSM.

REFERENCES

[1] The national energy administration press conference introduces the relevant energy situation in 2017, http://www.nea.gov.cn/2018-01/24/c_136921015.htm, accessed 24 Jan. 2018.

[2] In 2017, renewable energy generating 1.7 trillion KWH, www.nea.gov.cn/2018-01/26/c_136927061.htm, accessed 26 January 2018.

[3] H. Bevrani., T. Ise and Y. Miura, "Virtual synchronous generators: A survey and new perspectives," *Int. J. of Elect. Power & Energy Syst.*, Vol. 54, pp. 244-254, Jan. 2014.

[4] P. Tielens and D.-V. Hertem, "The relevance of inertia in power system," *Renew. and Sustain. Energy Reviews*,Vol. 55, pp.999-1009, Mar. 2016.

[5] J. Driesen and K. Visscher, "Virtual synchronous generators," in Proc. IEEE Power and Energy Soc. 2008 Gen. Meet.: Convers. Del. Energy 21 Century, Pittsburgh, PA, U.S.A, pp. 1-3, July. 2008.

[6] H.-P. Beck and R. Hesse, "Virtual synchronous machine," in *Proc. 9th Int. Conf. on Elect. Power Quality and Util., Barcelona, Spain*, pp.1-6, 2007.

[7] T. Loix, S. De Breucker, P. Vanassche, J. Van den Keybus, J. Driesen and K. Visscher, "Layout and performance of the power electronic converter platform for the VSYNC project," *IEEE PowerTech, Bucharest, Romania*, pp. 1-8, 2009.

[8] Q. C Zhong and G. Weiss, "Synchronverters: inverters that mimic synchronous generators," *IEEE Trans. Ind. Electron.*, Vol. 58, No. 4, pp. 1259-1267, Apr. 2011.

[9] J. Alipoor, Y. Miura, and T. Ise, "Power system stabilization using virtual synchronous generator with alternating moment of inertia," *IEEE J. Emerg. Sel. Topics Power Electron.*, Vol. 3, No. 2, pp. 451-458, Jun. 2015.

[10] A. Vassilakis, P. Kotsampopoulos, N. Hatziargyriou, and V. Karapanos, "A battery energy storage based virtual synchronous generator," *IREP Symp. Security and Control of the Emerging Power Grid, Rethymno, Greece* , pp.1-6, Aug. 2013.

[11] M. Albu, K. Visscher, D. Creanga, A. Nechifor, and N. Golovanov, "Storage selection for DG applications containing virtual synchronous generators," *IEEE Power Tech, Bucharest, Romania*, pp. 1-6, 2009.

[12] M. A. Torres L., L. A. C. Lopes, L. A. Morán T. and J. R. Espinoza C., "Self-tuning virtual synchronous machine: a control strategy for energy storage systems to support dynamic frequency control," *IEEE Trans. Energy Convers.*, Vol. 29, No. 4, pp 833-840, Dec. 2014.

[13] M. Benidris and J. Mitra, "Enhancing stability performance of renewable energy generators by utilizing virtual inertia," *IEEE Power and Energy Soc. Gen. Meet.,* pp. 1-6, 2012.

[14] M. Benidris, S. Elsaiah, S. Sulaeman and J. Mitra, "Transient stability of distributed generators in the presence of energy storage devices," *North American Power Symp., Champaign, IL, U.S.A.*, pp. 1-6, 2012.

[15] M. P. N. van Wesenbeeck, S. W. H. de Haan, P. Varela and K. Visscher, "Grid tied converter with virtual kinetic storage," *IEEE PowerTech, Bucharest, Romania*, pp. 1-7, 2009.

[16] J. Liu, J. Wen, W. Yao, and Y. Long, "Solution to short-term frequency response of wind farms by using energy storage systems," *IET Renew. Power Gener.*, Vol. 10, No.5, pp. 669-678, May. 2016.

[17] I. Serban, R. Teodorescu, and C. Marinescu, "Energy storage systems impact on the short-term frequency stability of distributed autonomous microgrids, an analysis using aggregate models," *IET Renew. Power Gener.*, Vol. 7, No. 5, pp. 531-539, Sep. 2013.

[18] S. Wang, J. Hu, X. Yuan, and L. Sun, "On inertial dynamics of virtual synchronous controlled DFIG-based wind turbines," *IEEE Trans. Energy Convers.*, Vol. 30, No. 4, pp. 1691-1702, Dec. 2015.

[19] S. D'Arco and J. A. Suul, "Equivalence of virtual synchronous machines and frequency-droops for converter-based microgrids," *IEEE Trans. Smart Grid*, Vol. 5, No. 1, pp. 394-395, Jan. 2014.

[20] S. D'Arco and J. A. Suul, "Virtual synchronous machines -- classification of implementations and analysis of equivalence to droop controllers for micro-grids," *IEEE Power Tech, Grenoble, France*, pp. 1-7, 2013.

[21] L. Xiong, F. Zhuo, F. Wang, X. Liu, Y. Chen, M. Zhu, and H. Yi, "Static Synchronous generator model: A new perspective to investigate dynamic characteristics and stability issues of grid-tied PWM inverter," *IEEE Trans. Power Electron.*, Vol. 31, No.9, pp. 6264-6280, Sep. 2016.

[22] J. Liu, Y. Miura, and T. Ise, "Comparison of dynamic characteristics between virtual synchronous generator and droop control in inverter-based distributed generators," *IEEE Trans. Power Electron.*, Vol. 31, No. 5, pp. 3600-3611, May 2016.

[23] P. Kundur, *Power System Stability and Control*, McGraw Hill, chap. 3, pp.129, 1994.

Chang Yuan was born in Hunan, China, in 1981. He received his B.S. and Ph.D. degrees in Electrical Engineering from Xi'an Jiaotong University, Xi'an, China, in 2003 and 2010, respectively. He is presently working as a Lecturer in the North China Electric Power University, Beijing, China. His current research interests include power electronics applied to power systems.

Chang Liu was born in Shandong, China, in 1992. He received his B.S. degree from the Shanghai University of Electric Power, Shanghai, China, in 2014; and his M.S. degree from the North China Electric Power University, Beijing, China, in 2017. He is presently working at the State Grid Jinan Power Supply Company, Jinan, China.

Dan Yang was born in Shanxi, China, in 1994. She received her B.S. degree from the North China Electric Power University, Baoding, China, in 2016. She is presently working towards her M.S. degree at the North China Electric Power University, Beijing, China. Her current research interests include power electronics applied to power systems.

Niang Tang was born in Hunan, China, in 1984. He received his B.S. and M.S. degrees in Electrical Engineering from the Changsha University of Science and Technology, Changsha, China, in 2006 and 2009, respectively. He received his Ph.D. degree in Electrical Engineering from the North China Electric Power University, Beijing, China, in 2013. He is presently working as an Engineer at the Electric Power Research Institute of the Guangdong Power Grid Co., Ltd., Guangzhou, China. His current research interests include power electronics and power quality.

Ruibing Zhou was born in the Inner Mongolia Autonomous Region, China, in 1990. He is presently working towards his M.S. degree in Electrical Engineering at the North China Electric Power University, Beijing, China. His current research interests include the application of new transmission technologies in power systems.